



RANS investigation of influence of wave steepness on ship motions and added resistance in regular waves

Si Chen^{1,2,4} · Takanori Hino³ · Ning Ma^{1,2,3,4} · Xiechong Gu^{1,2,4}

Received: 1 May 2017 / Accepted: 24 December 2017 / Published online: 12 January 2018
© JASNAOE 2018

Abstract

The motions and added resistance of the S175 containership in regular head waves with different wave steepness under the same wavelength are investigated using a Reynolds-averaged Navier–Stokes solver based on a finite-volume method. A level set method is used to capture the free surface and dynamic grids are adopted to simulate ship motions. The variation of heave and pitch motions and added resistance with the wave steepness agrees with the experiment. The higher harmonic components of surge force obtained by the Fourier analysis increase dramatically as the wave steepness increases, while the higher harmonics of heave and pitch are quite small compared to the first harmonics even under large wave steepness. The transient pressure distributions are studied to explain the non-harmonic oscillations of the time history of resistance coefficient. The zeroth, first, and second harmonic amplitudes of pressure are plotted on the hull and the major part of resistance increase in steeper waves is found to be induced at the bow.

Keywords Added resistance · Ship motions · Wave steepness · RANS

1 Introduction

Added resistance in waves is one of the main components of the total resistance of ships in the actual sea states. Estimation of added resistance is important for the design of the propulsion system of a ship and for the prediction of the fuel consumption during actual operations. Recently, with the implementation of the IMO regulations about Energy Efficiency Design Index [1], added resistance calculation methods with higher precision are needed for the optimization of energy efficiency. Furthermore, the evaluation of added resistance in steep waves is essential for the calculation of Minimum Propulsion Power which is required in the IMO regulation [2]. Wave steepness has been proved to have

a significant nonlinear influence on added resistance in the experiment [3] which shows that the added resistance coefficient in high waves is 18–44% less than that of low waves. Therefore, wave steepness should be considered in the added resistance calculation methods and the influence of wave steepness should be investigated.

Nowadays, the conventional method to calculate added resistance is the potential flow method which can be categorized into the far-field method and the near-field method. In the far-field method, added resistance is evaluated based on the consideration of the energy and momentum relation in the far field. Early attempts to calculate added resistance were performed with a strip method [4–6]. With the development of 3D potential flow methods, the far-field formulation was applied with a 3D panel method [7, 8]. The near-field method, on the other hand, obtains added resistance by integrating the pressure on the hull surface. It can be carried out by means of a strip method [9], or a 3D panel method [10]. Recently, the middle-field method, which obtains added resistance from a control surface near the hull, is introduced and added resistance can be estimated with the application of a Green Function panel method [11] or a Rankine Source panel method [12].

The potential flow method is established following the perturbation procedure, in which the boundary conditions

✉ Ning Ma
ningma@sjtu.edu.cn

¹ State Key Laboratory of Ocean Engineering, Shanghai Jiao Tong University, Shanghai, China

² Collaborative Innovation Center for Advanced Ship and Deep-Sea Exploration, Shanghai, China

³ Institute of Advanced Sciences, Yokohama National University, Yokohama, Kanagawa, Japan

⁴ School of Naval Architecture, Ocean and Civil Engineering, Shanghai Jiao Tong University, Shanghai, China

are linearized based on the assumption of the small oscillations of boundaries. The added resistance problem is treated as a second-order problem and the added resistance obtained is proportional to the square of wave amplitude. Therefore, the potential flow method is theoretically valid for small wave steepness only. More comprehensive methods with different levels of complexity have been presented and modifications have been made to include nonlinear terms such as a nonlinear body condition, a nonlinear-free surface condition, and a nonlinear wave model. However, these modifications are too complicated to be implemented in the calculation of added resistance. Recently, a simplified method to include the wave steepness in the added resistance calculation is presented by introducing the nonlinear wave excitation force [13]. Despite the continuous development of the potential flow method, due to the basic assumption of inviscid and irrotational flow, the potential flow method cannot be used to treat strongly nonlinear problems such as breaking waves which often happen in steep waves.

With the rapid development of CFD technique, the resistance of ships sailing in waves can be obtained through CFD simulations [14–17]. Extensive studies on seakeeping were carried out in the Gothenburg 2010 workshop [18]. A variety of CFD solvers with different turbulence models, free surface modeling methods, discretization methods, and grid types were adopted in these studies. In general, the CFD methods gave better results than the potential flow approaches. The motions and mean resistance fairly agreed with the experiment, while large errors were observed for the first-order harmonic amplitude of surge force. Most of the simulations were carried out under a series of wave frequencies and the influence of wave steepness was not examined except that Shen [19] evaluated the added resistance of the DTMB model 5512 with different wave steepness and strongly nonlinear features were observed. Compared to potential flow methods, CFD methods based on Navier–Stokes equations can deal with problems in steep waves and the flow details which help to understand the nonlinear features can also be obtained.

In this paper, the heave and pitch motion and added resistance for the S175 containership are calculated using a Reynolds-averaged Navier–Stokes (RANS) solver developed by Hino [20, 21]. The focus is the nonlinear behavior of the added resistance in steep waves, so the simulations are carried out at one wavelength with a wide range of wave steepness. The calculated results for added resistance and ship motions are validated using the published experimental data. The higher order harmonic amplitudes are obtained by means of Fourier series to analyze the nonlinear characteristics. The pressure distributions on hull surface are studied to understand the non-harmonic oscillations of the resistance coefficient.

2 Numerical methods

The governing equations are the RANS equations with the introduction of artificial compressibility. With all variables non-dimensionalized by the reference length L_0 , reference velocity U_0 , and fluid density ρ_0 , the RANS equations can be expressed in the integral form as follows:

$$\frac{d}{d\tau} \iiint_{\Omega} \mathbf{q} dV + \frac{d}{dt} \iiint_{\Omega} \mathbf{J} \mathbf{q} dV + \iint_{\partial\Omega} [(\tilde{\mathbf{e}} - \mathbf{e}^v)n_x + (\tilde{\mathbf{f}} - \mathbf{f}^v)n_y + (\tilde{\mathbf{g}} - \mathbf{g}^v)n_z] dS = 0, \quad (1)$$

where τ denotes the pseudo-time and t denotes the physical time used in the dual time stepping described below. \mathbf{J} is a diagonal matrix defined as $\text{diag}(0, 1, 1, 1)$. \mathbf{q} is the vector of the flow variables defined as

$$\mathbf{q} = \begin{bmatrix} p \\ u \\ v \\ w \end{bmatrix}, \quad (2)$$

where (u, v, w) are the (x, y, z) components of the velocity of fluid and p is the modified pressure from which the hydrostatic component is extracted, that is

$$p = p^* + \frac{z}{Fn^2}, \quad (2)$$

where p^* is the original pressure and Fn is the Froude number defined as $U_0/\sqrt{gL_0}$. The inviscid fluxes $\tilde{\mathbf{e}}$, $\tilde{\mathbf{f}}$, and $\tilde{\mathbf{g}}$ are given by

$$[\tilde{\mathbf{e}} \ \tilde{\mathbf{f}} \ \tilde{\mathbf{g}}] = \begin{bmatrix} \beta u & \beta v & \beta w \\ u(u - u_g) + p & u(v - v_g) & u(w - w_g) \\ v(u - u_g) & v(v - v_g) + p & v(w - w_g) \\ w(u - u_g) & w(v - v_g) & w(w - w_g) + p \end{bmatrix}, \quad (3)$$

where β is a parameter for artificial compressibility and (u_g, v_g, w_g) are the (x, y, z) components of the grid velocity of the surfaces S of the control volume V . The viscous fluxes \mathbf{e}^v , \mathbf{f}^v , and \mathbf{g}^v are given by

$$[\mathbf{e}^v \ \mathbf{f}^v \ \mathbf{g}^v] = \begin{bmatrix} 0 & 0 & 0 \\ \tau_{xx} & \tau_{xy} & \tau_{xz} \\ \tau_{yx} & \tau_{yy} & \tau_{yz} \\ \tau_{zx} & \tau_{zy} & \tau_{zz} \end{bmatrix} \quad (4)$$

where $\tau_{x_i x_j}$ ($i, j = 1, 2, 3$) is defined as

$$\tau_{x_i x_j} = \left(\frac{1}{Rn} + \nu_t \right) \left(\frac{\partial u_i}{\partial x_j} + \frac{\partial u_j}{\partial x_i} \right), \quad (5)$$

where ν_t is the non-dimensional kinematic eddy viscosity and Rn is the Reynolds number defined as $U_0 L_0 / \nu$, where ν is the kinematic viscosity. ν_t can be obtained by a specific

turbulence model. In the present work, $k - \omega$ SST turbulence model [22] is used except for the case with the largest wave steepness in which the $k - \omega$ SST turbulence model fails and the Spalart–Allmaras turbulence model [23] is used instead. The calculation results with two turbulence models for lower wave steepness are almost the same. Therefore, Spalart–Allmaras model is considered to be as accurate as $k - \omega$ SST in this study.

A finite-volume method is adopted for spatial discretization [20]. The second-order upwind scheme is used for the inviscid flux and the second-order central difference scheme for the viscous flux. Velocity–pressure coupling is achieved based on the artificial compressibility concept in which the divergence-free condition is satisfied in the steady-state limit. To apply the artificial compressibility method to unsteady problems, dual time stepping [24] is adopted, in which pseudo-time iterations are performed until the divergence-free condition is satisfied at each physical time step. The second-order two-step backward scheme and the first-order Euler implicit scheme are used for the physical time stepping and pseudo-time stepping, respectively. In the present study, the dual time stepping is used in simulations in incident waves. A calm water case is regarded as a steady problem in which only the pseudo-time stepping is applied.

A level set method [21] is adopted to capture the free surface. In calm water conditions, to avoid the reflection of the free surface waves at the outer boundaries of the computational domain, a damping term is included in the solution. In wave conditions, the flow variables near the boundaries are set identical to the analytical formulation of the linear wave theory and they are blended with the inner flow field solved from the governing equations [25].

The motion equations are coupled with the dual time stepping through the third-order Adams–Bashforth/Adams–Moulton scheme [26]. The grids whose distance from the hull surface is $0.3L_{pp} \sim 0.7L_{pp}$ are deformed at each time step fitting to the current position and attitude of the ship hull.

3 Geometry and simulation conditions

The S175 containership is used in the simulations, because the experimental data under different wave steepness are available for this ship [3]. A ship model of a scale of 1:43.75 is used in the experiment and the same model is used in the simulation. Principal particulars of the S175 containership are listed in Table 1.

The freeboard is extruded vertically upward from the deck to increase the stability of simulations. This manner will eliminate the green water phenomenon in steep waves and cause calculation errors. However, the agreement with

Table 1 Principal particulars of the S175 containership model

Parameters		Ship model
Length between perpendiculars	L_{pp} (m)	4.0000
Breadth	B (m)	0.5847
Draft at forward perpendicular (F.P.)	d_F (m)	0.1952
Draft at aft perpendicular (A.P.)	d_A (m)	0.2199
Displacement	∇ (m ³)	0.2769
Longi. center of buoyancy from F.P.	LCB (% L_{pp})	0.5200
Longi. radius of gyration	k_{yy} (% L_{pp})	0.2400
Height of C.G. above base line	KG (m)	0.1778

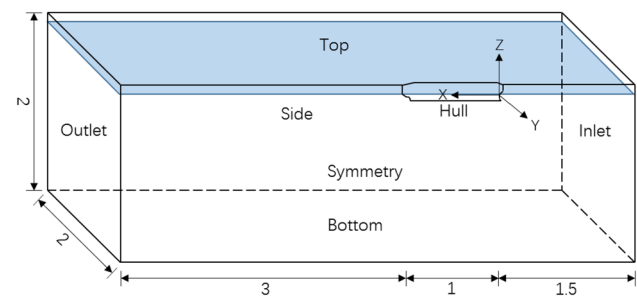


Fig. 1 Computational domain

the experiment implies that the green water may have a small impact on the final results.

The simulation conditions are selected according to the experimental conditions. Five cases in regular head waves and a calm water case are carried out. The Froude number Fn is set to 0.25 for all cases and the wavelength λ is $0.9L_{pp}$ for the cases in waves. The ratio of wave height to wavelength, H/λ , is 0.011, 0.022, 0.033, 0.044, and 0.056, respectively. The ship is free to heave, pitch, and surge in the experiment. However, the details of the spring system are unknown and the influence of surge motion is small [27, 28]. Therefore, the surge motion is ignored in the simulations.

4 Computational domain, boundary conditions, and grids

The computational domain is a rectangular domain, as shown in Fig. 1. The domain is non-dimensionalized by L_{pp} . The origin of the coordinate system coincides with the forward perpendicular on the free surface and the x -axis is oriented from bow to stern. The y -axis is positive to star board with z -axis pointing upward. The computational domain extends from $-1.5 < x < 4.0$, $-2.0 < y < 0.0$ and $-2.0 < z < 0.2$ for all cases. The no-slip boundary condition is applied on the hull surface and the symmetry condition is

imposed on $y=0$. For the inlet, the inflow velocity is specified, and for the outlet, top, side, and bottom, the pressure and the velocity are extrapolated except that the pressure is specified on the outlet boundary.

In the calm water condition, the wave damping zone shown in Fig. 2 is set at the inlet, side, and outlet to avoid the reflection of waves. The width of the wave damping zone is 0.5. In wave conditions, the flow variables are set identical to the analytical solution for linear waves in the wave generating zone shown in Fig. 3 and they are blended gradually with the inner flow field in the blending zone. The width of the wave generating zone and blending zone is both 0.25.

Unstructured hexahedral grids are used in the present study and boundary layer grids are generated on the hull surface with the minimum spacing on the wall being 5×10^{-6} . Grid refinement is required near the free surface and in the Kelvin wave region to resolve the incident waves and the ship generated waves well. The grids are also refined near the hull to obtain the flow details.

The grid size of the flow field is determined by the requirement of the incident wave modeling. The wave height usually reduces gradually as waves propagate due to numerical dissipation. The decay rate of waves is relevant to the grid size near the free surface. To obtain the suitable grid size, a series of grid-dependence tests are performed. In these simulations, the ship hull is extracted from the computational domain and the dimension in y direction is reduced to save the computing time while keeping the same in x and z directions. The other parameters for simulations are $Fn = 0.25$, $\lambda = 0.9L_{pp}$, and $H = 0.033\lambda$.

The results are shown in Table 2. λ/dx and H/dz denote the subdivisions of wavelength and wave height, which means how many cells are divided into one wavelength and one wave height. H'/H denotes the ratio between the simulated wave height measured at the aft perpendicular and the desired wave height which is an input parameter. The results indicate that wave decay is more sensitive to the subdivision of wavelength and the decay rate is much slower with a denser subdivision of wavelength. The subdivision of wave

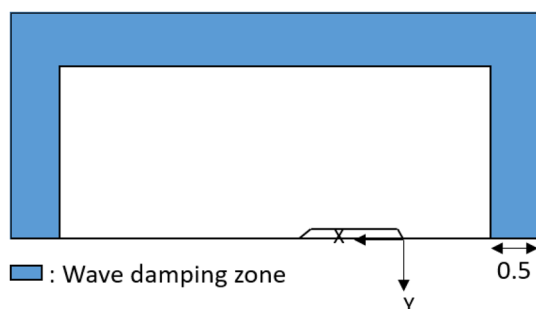


Fig. 2 Wave damping zone viewed from top

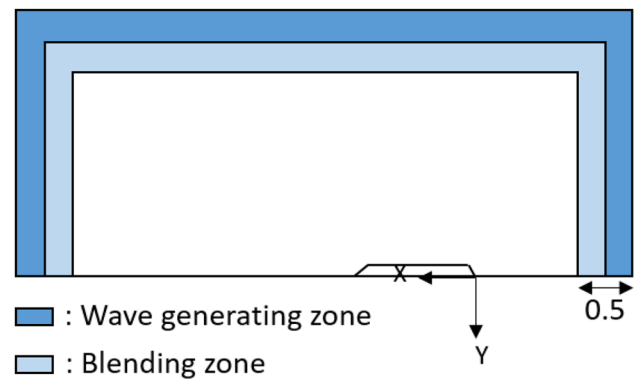


Fig. 3 Wave generating zone and blending zone viewed from top

height makes smaller differences on the results compared to wavelength.

$\lambda/dx = 200$ and $H/dz = 10$ are used in the following simulations out of the consideration of the balance between accuracy and efficiency. $H/dz = 10$ is kept for all wave cases, which means that the height of grids varies with wave height. The grids viewed from three directions for the case is shown in Figs. 4, 5, and 6, respectively. As shown in Fig. 4, $\lambda/dx = 200$ is applied in front of the ship, along with the ship, and down to one ship length behind the ship. Behind that $\lambda/dx = 100$ is used, because the wave propagation downstream of the ship has less influence on the issues concerned. Besides, the grid refinement mentioned above is observed in the Kelvin wave region and very fine grids can also be observed near the free surface and hull surface in Figs. 5 and 6.

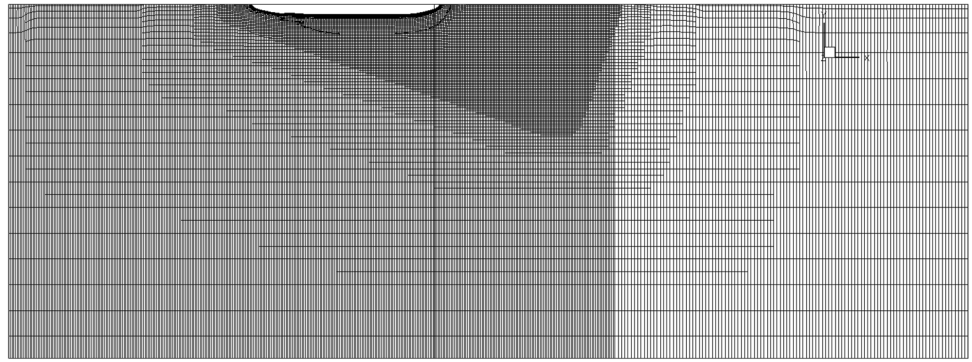
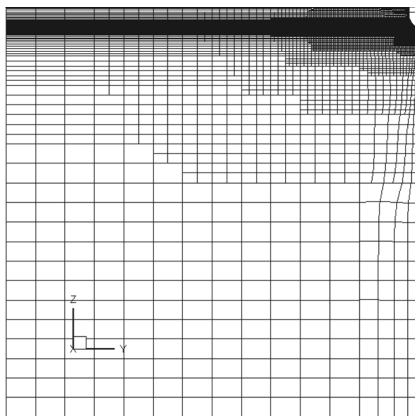
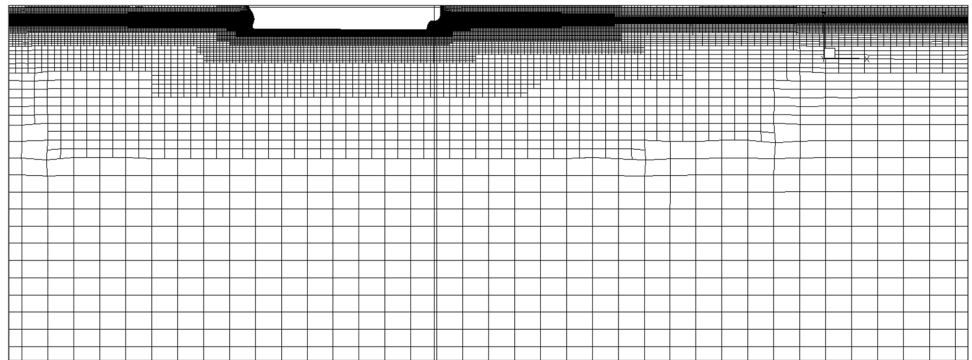
5 Results and discussion

5.1 Time histories of wave elevation, ship motions, and resistance coefficient

The total simulation time is $15T_e$, where T_e is the encounter period. After about $5T_e$, the system reaches a steady periodically changing state. Time histories of wave elevation, heave, pitch, and resistance coefficient in one encounter period are

Table 2 Results of grid-dependence tests for incident wave modeling

Case no.	λ/dx	H/dz	H'/H
1	100	10	0.7219
2	100	20	0.7303
3	150	10	0.8598
4	150	20	0.8695
5	200	5	0.8557
6	200	10	0.9036
7	200	20	0.9142

Fig. 4 Grids of slice located at $z=0.07$ **Fig. 5** Grids of slice located at $y=0$ **Fig. 6** Grids of slice located at $x=1$

shown in Fig. 7. Wave elevation ζ and heave motion ξ_3 are non-dimensionalized by L_{pp} . Pitch motion ξ_5 is expressed in rad. The resistance coefficient C_t is defined as

$$C_t = F_x / (0.5 \rho U^2 L_{pp}^2), \quad (6)$$

where F_x is the measured external force of the ship in x direction (the total resistance of the ship). Note that the time history of the wave elevation is recorded at a point which has the same x coordinate as F.P., but shifts $1.0L_{pp}$ away from

$y=0$ in y direction, so that the disturbance caused by the ship can be neglected.

For heave and pitch, harmonic oscillations with the period conforming to those of incident waves are observed. For resistance coefficient, the oscillations are harmonic approximately only for the case with the smallest wave steepness. Nonlinear characteristics arise and are enhanced with the increase of wave steepness.

5.2 Computation of mean value

The results shown in Fig. 7 are analyzed by means of Fourier series. n th ($n \geq 0$) harmonic amplitudes of ζ , ξ_3 , ξ_5 , and F_x will be denoted as $\zeta^{(n)}$, $\xi_3^{(n)}$, $\xi_5^{(n)}$, and $F_x^{(n)}$. $F_x^{(0)}$ represents the mean resistance in waves and $F_x^{(n)}$ ($n \geq 1$) represents the n th harmonic amplitude of the surge exciting force.

It is found that the mean value cannot be evaluated precisely by means of Fourier series in one period, especially under small wave steepness. Figure 8a shows the time histories of wave elevation, heave, pitch, and resistance coefficient for the case $H/\lambda = 0.011$. After a transition phase in which the waves propagate to the measurement point, the wave elevation begins to vary periodically. However, there is a low-frequency disturbance, whose period is about 5–6 times of the wave period due to numerical error. It induces the low-frequency variation of heave, pitch, and especially the resistance coefficient, which is

Fig. 7 Time histories in one encounter period: a wave elevation, b heave, c pitch, and d resistance coefficient

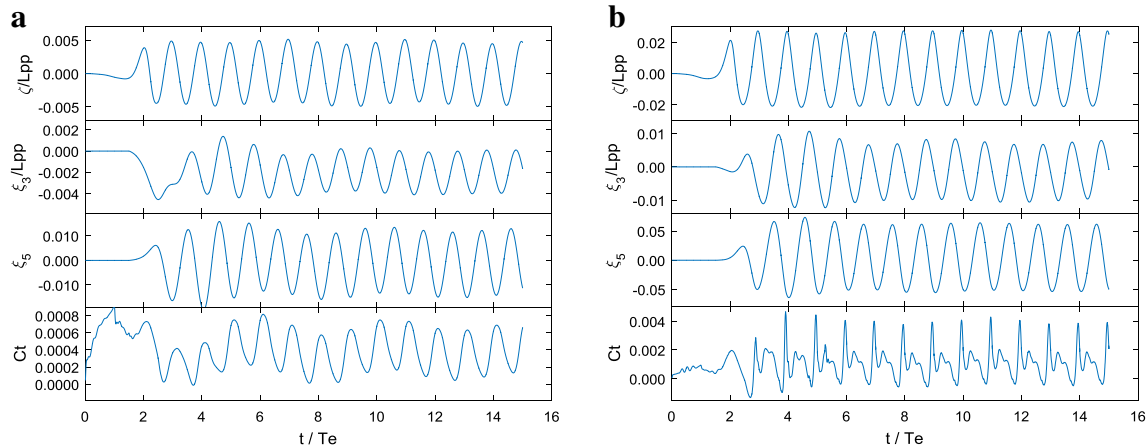
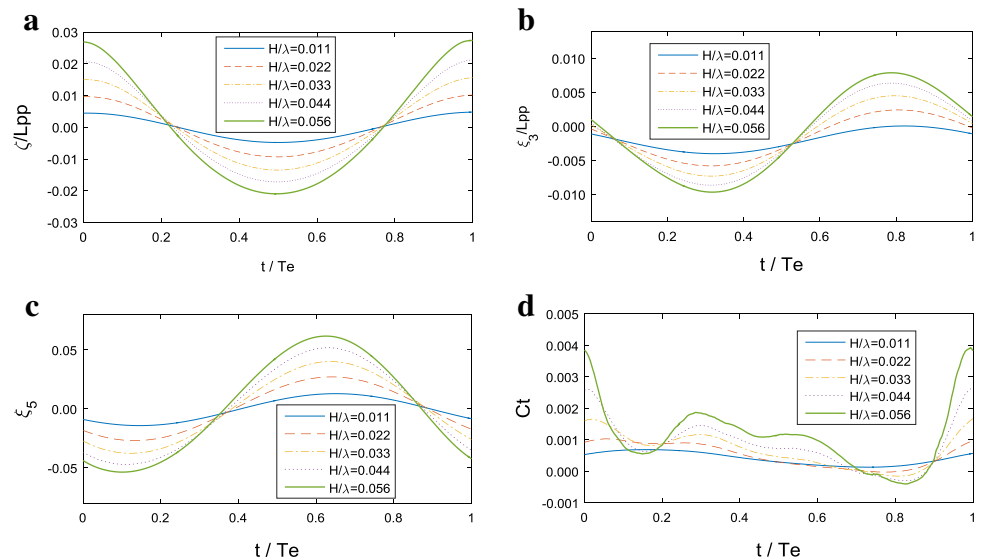


Fig. 8 Time histories of wave elevation, heave, pitch, and resistance coefficient. **a** $H/\lambda = 0.011$, **b** $H/\lambda = 0.056$

more sensitive to wave elevation and also influenced by ship motions. Then, the computation of $F_x^{(0)}$ will depend on the selection of the time window, in which F_x is time-averaged. The low-frequency oscillations also exist for larger wave steepness, as shown in Fig. 8b. However, as the wave steepness increases, the amplitudes of wave elevation, motions, and resistance coefficient also increase and the influence of low-frequency oscillation is relatively small. The grid-dependence tests show that the low-frequency component cannot be eliminated by increasing the number of the mesh, but it will gradually decay with time going on. However, it will cost too much time when the low-frequency oscillation finally vanishes.

To reduce the error caused by the low-frequency oscillation, $F_x^{(0)}$ is determined in the following way. $F_x^{(0)}$ computed from the time window, whose length is one encounter period, is plotted in Fig. 9, in which $t1$ represents the start

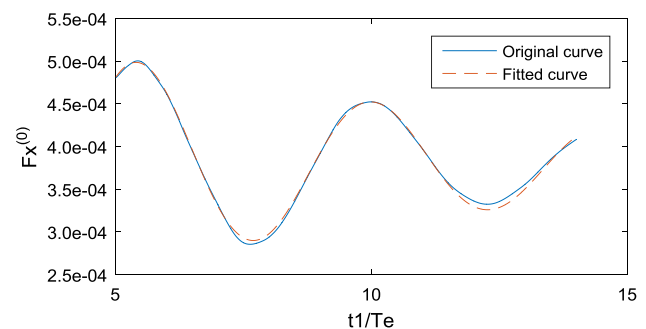


Fig. 9 Variation of $F_x^{(0)}$ with the start point of time window

point of the time window. $t1$ is selected at every time instant, while the length of the time window keeps the same. The curve can be approximated as a function in the following form:

$$F_x^{(0)} = a + be^{-c} \cos\left(\frac{2\pi}{d}t + e\right), \quad (7)$$

in which a , b , c , d , and e are determined by nonlinear least squares method. The fitted curve is also plotted in Fig. 9. $F_x^{(0)}$ is assumed to follow the trend of the fitted curve with time going on. The fitted curve will finally converge at the coefficient a , which is the mean resistance expected. Because the form of the fitted curve is assumed based on the time history of $10 T_c$ which is not long enough, there is still some error caused by low-frequency oscillation. However, this method can reduce the error to a great extent.

5.3 Validation of the computational results

The results of the non-dimensional first harmonic amplitudes of heave and pitch and the added resistance coefficient are shown in Fig. 10. The horizontal axis represents the actual wave steepness defined as H'/λ , where H' represents the measured wave height defined as $2\zeta^{(1)}$. H' should be distinguished from H which is an input parameter of the simulation. The non-dimensional first harmonic amplitudes of heave and pitch will be non-dimensionalized by $\zeta^{(1)}$ and $k\zeta^{(1)}$, where k is the wave number. Added resistance R_{AW} is calculated by

$$R_{AW} = F_x^{(0)} - F_x^{(\text{Calm})}, \quad (8)$$

where $F_x^{(\text{Calm})}$ represents the calm water resistance which is computed using the same CFD method. The added resistance coefficient is defined as

$$C_{AW} = R_{AW} / \left(\rho g (\zeta^{(1)})^2 B^2 / L_{pp} \right). \quad (9)$$

Both the computational and experimental results for the non-dimensional first harmonic amplitudes of heave and pitch and the added resistance coefficient shows a decreasing trend with the increase of wave steepness and the matching between calculation and experiment is quite satisfying. It indicates that the present CFD method has the capability to calculate motions and resistance of ships in steep waves and the influence of wave steepness can be considered effectively. It should be noted that the trends of ship motions and added resistance may be frequency dependent and the trends may be different at other frequencies.

Besides the difference of amplitude of heave and pitch shown in Fig. 10, there is also difference of phase among cases with different wave steepness. The phase lags between first harmonics of ship motions and first harmonics of wave elevation at F.P. are plotted in Fig. 11 and a difference about 10° can be observed for the phase lags. However, there is no experimental data about the phase.

5.4 Higher harmonic components

The higher harmonic behaviors are analyzed by comparing higher harmonic amplitudes with the first harmonic amplitudes. The results for heave, pitch, and surge force are shown in Fig. 12. The higher harmonic amplitudes for heave and pitch are significantly smaller than the first harmonics even in the highest waves. For the surge force, the higher

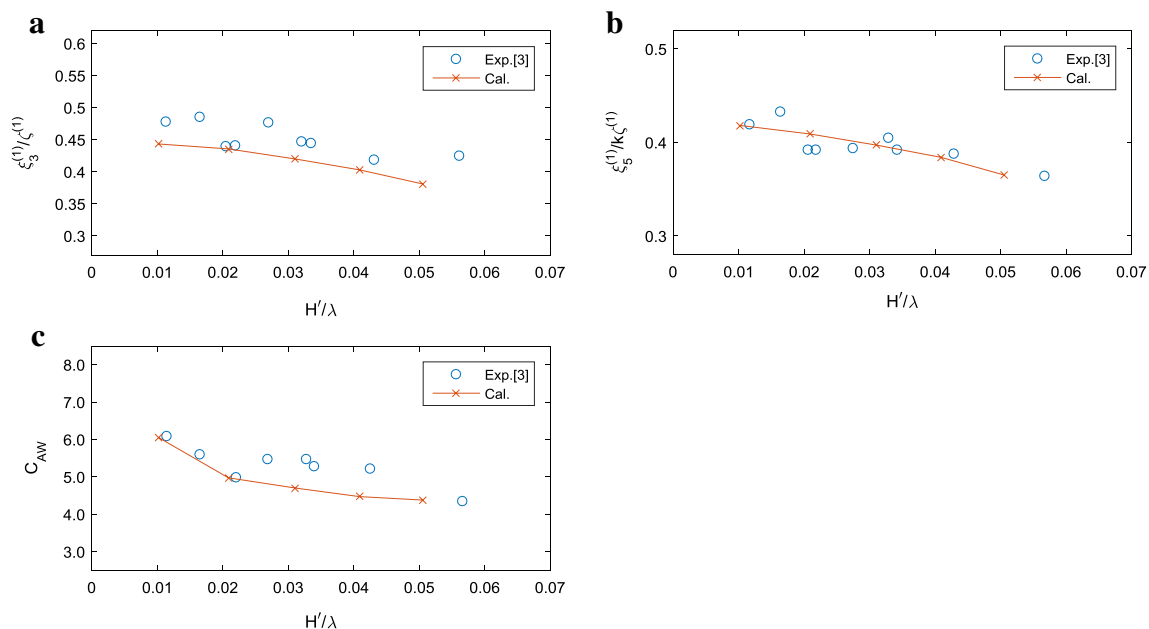


Fig. 10 Comparison with the experimental data. **a** non-dimensional first harmonic amplitudes of heave, **b** non-dimensional first harmonic amplitudes of pitch, **c** added resistance coefficient

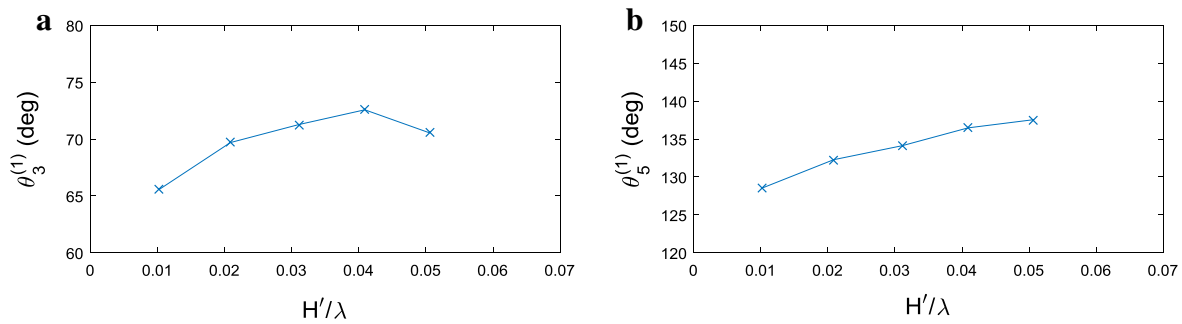


Fig. 11 Phase lags between first harmonics of ship motions and first harmonics of wave elevation at F.P. **a** heave, **b** pitch

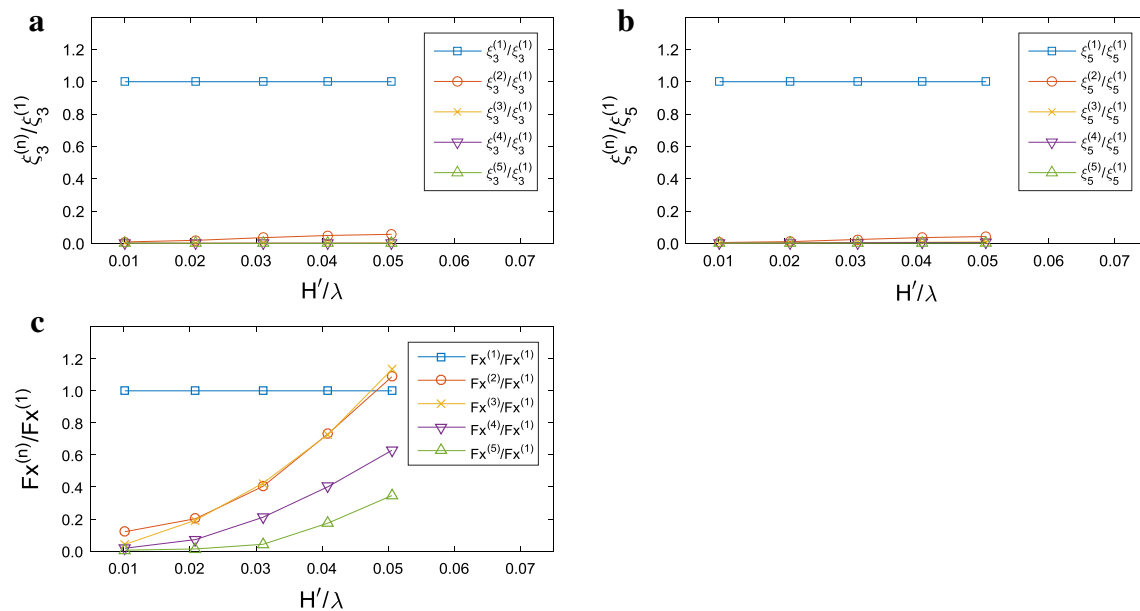


Fig. 12 Ratio of higher harmonic amplitudes and first harmonic amplitude. **a** heave, **b** pitch, **c** surge force

harmonic amplitudes are small compared to the first harmonics only in cases with the smallest wave steepness. The higher harmonic amplitudes increase rapidly as the wave steepness grows. The second and third harmonic amplitudes are even larger than the first harmonic amplitude in the largest wave steepness case. The third harmonic component is smaller than the second harmonics only under the smallest wave steepness. For cases with larger wave steepness, the third harmonic amplitude is almost the same as the second harmonics.

The potential flow method to calculate added resistance is established based on the assumption of a small steepness of incident waves. A perturbation solution in terms of this small parameter is adopted to obtain the surge force of different orders. The second and third harmonic surge forces are regarded as higher order small values and should be much smaller than the first harmonic. However, the simulation

results show that the amplitudes of the second and third harmonic surge forces are almost as large as the first harmonic in cases with large wave steepness. Such nonlinearity may be beyond the scope of the perturbation solution adopted in the potential flow method.

5.5 Pressure distribution

To explain the non-harmonic variations of the time history of resistance coefficient, the pressure distribution at each time step is studied. First, time histories of wave elevation, heave, pitch, and resistance coefficient for the case $H/\lambda = 0.056$ in one encounter period are drawn in Fig. 13. Noted that the time history of wave elevation is recorded at a point which has the same x coordinate as the F.P., but shifts $1.0L_{pp}$ away from the F.P. in y direction. The start time of one

period is selected in the way that the wave crest is located at the F.P. at $t/T_e = 0$.

Resistance coefficient reaches its maximum at $t/T_e \approx 0$ and minimum at $t/T_e \approx 0.8$. In addition, there is a local minimum at $t/T_e \approx 0.15$ and a local maximum at

$t/T_e \approx 0.3$. The pressure distributions on the hull surface for these time steps are drawn in Fig. 14. The contour represents the x component of the pressure p^* in Eq. (2). The bold curve in blue color near the free surface is the wave profile on the hull. Figure 15 shows the resistance

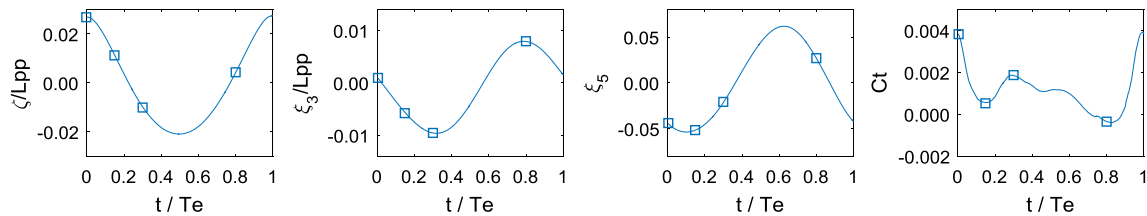


Fig. 13 Time histories of wave elevation, heave, pitch, and resistance coefficient in one encounter period

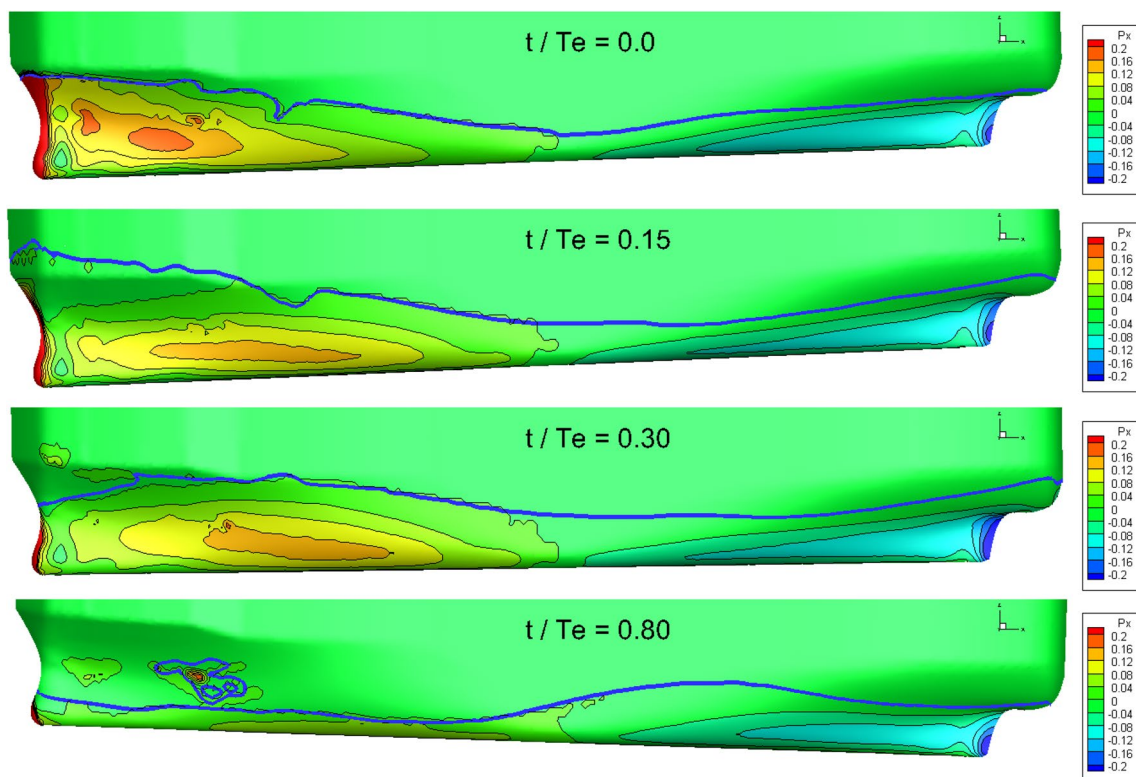
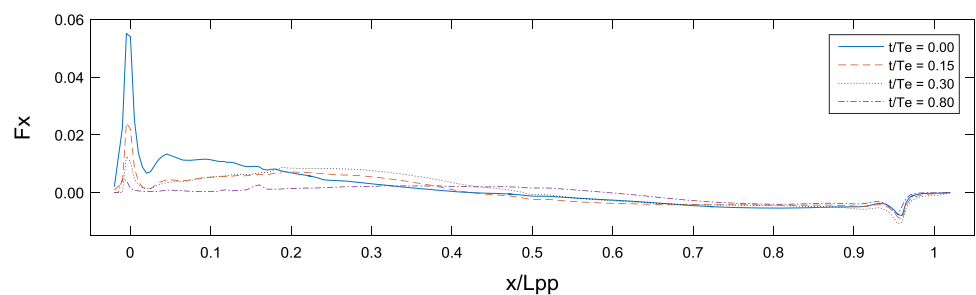


Fig. 14 X component of pressure at $t/T_e = 0, 0.15, 0.3, 0.8$ for the case $H/\lambda = 0.056$

Fig. 15 Resistance distributions along x -axis at $t/T_e = 0, 0.15, 0.3, 0.8$ for the case $H/\lambda = 0.056$



distribution along the ship. F_x is the x component of the integral of the pressure p^* along each section. The horizontal axis represents the x coordinate of each section.

At $t/T_e \approx 0$, the wave crest is located at the bow and the pitch is approaching the maximum bow-down. Very high pressure is observed at the bow in Fig. 14. The high pressure and large immersed area at the bow make significant contribution to the resistance which can be confirmed in Fig. 15. At $t/T_e \approx 0.15$, a local minimum value occurs. As shown in Fig. 14, the wave crest moves a little towards the stern and the pressure at the bow decreases significantly compared to $t/T_e \approx 0$. At $t/T_e \approx 0.3$, the resistance coefficient reaches a local maximum value. The wave crest continues to move to stern and the downward heave maximum is reached (see Fig. 13) which means that the largest area of wetted surface can be expected. The minimum value of resistance is obtained at $t/T_e \approx 0.8$ which is correspond to the largest upward heave motion (see Fig. 13). It is shown in Fig. 14 that very small hull surface immerses in the water and no obvious high-pressure region is observed. This causes the minimum resistance.

To summarize, the non-harmonic fluctuations of the time history of the resistance coefficient result from the nonlinear interactions between ship motions and waves. The pressure on the wetted surface varies dramatically both in space and time, especially near the bow. The wetted surface also

changes violently as a result of the wave propagation and ship motions. The phase difference between ship motions and incident waves plays an important role.

According to the perturbation solution adopted in the potential flow theory, the variation of wetted hull surface should be small. Then only the velocity potential on the mean wetted hull surface needs to be solved and the influence of the hull shape above the mean waterline cannot be considered. However, the visualization of the wave profile on the hull shows that the variation of wetted surface is so violent that the influence of the flare shape cannot be ignored. There is also other strongly nonlinear phenomenon which cannot be considered in the potential flow theory, such as the breaking waves at the bow. The conventional potential method cannot consider these factors and may give inaccurate prediction of added resistance under large wave steepness. More precise methods, such as the present method, are needed to solve these problems.

Figure 16 shows the time-averaged x component of pressure for the calm water case and three cases in waves. Figure 17 shows the time-averaged resistance distributions along x -axis. \bar{F}_x represents the time-averaged value of F_x in one period. It can be observed in Fig. 16 that the high-pressure area near the bow become larger gradually with the increase of wave steepness. In Fig. 17, four curves are almost coincident except in the region of $x/L_{pp} < 0.2$ and

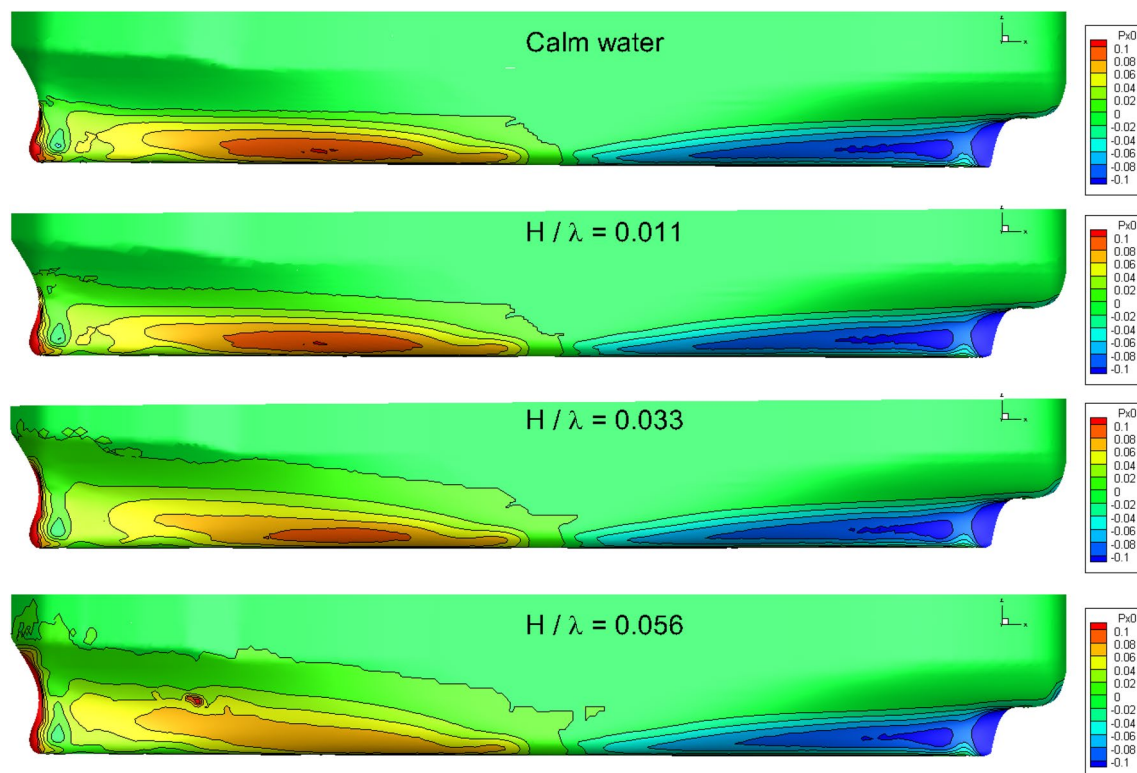


Fig. 16 Time-averaged x component of pressure for the calm water case and three cases in waves ($H/\lambda = 0.011, 0.033, 0.056$)

$0.5 < x/L_{pp} < 0.7$. The most significant difference is found at the positive peak near the bow. These results indicate

that the major part of resistance increase in steeper waves is induced near the bow. Figures 18 and 19 show the first and

Fig. 17 Time-averaged resistance distributions along x -axis for the calm water case and three cases in waves ($H/\lambda = 0.011, 0.033, 0.056$)

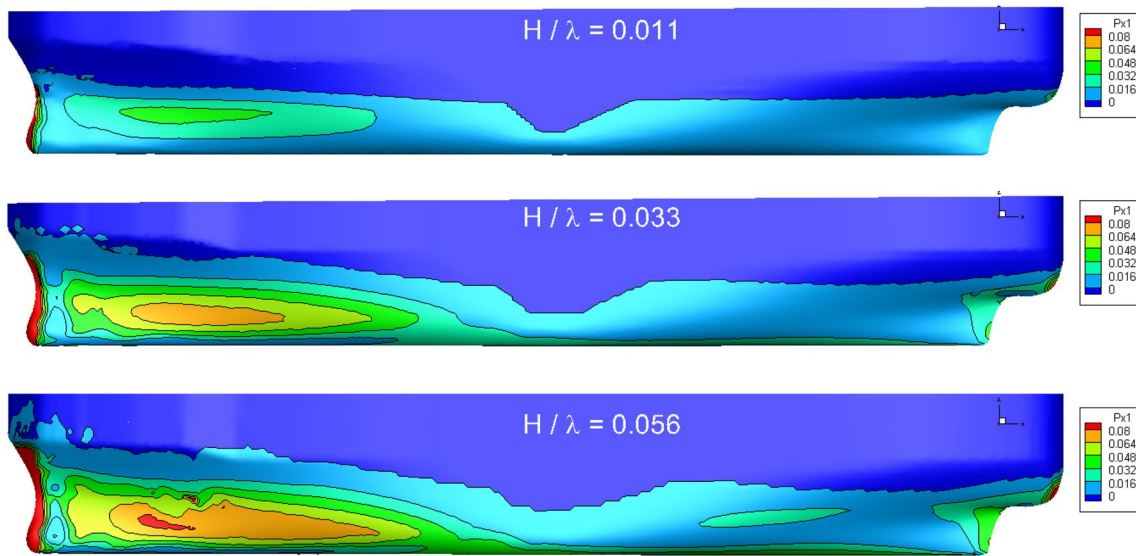
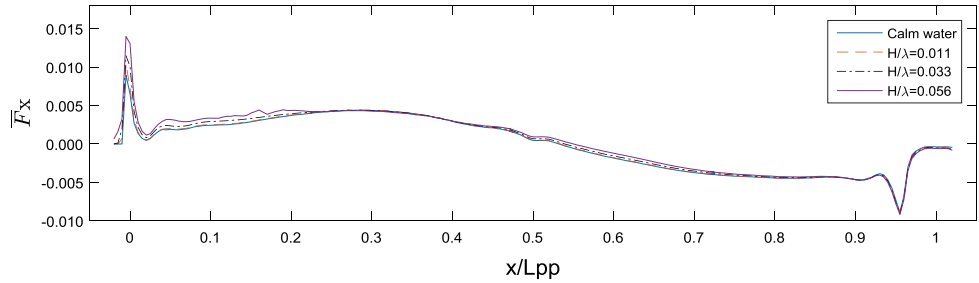


Fig. 18 First harmonic amplitude of the x component of pressure for the case $H/\lambda = 0.011, 0.033, 0.056$

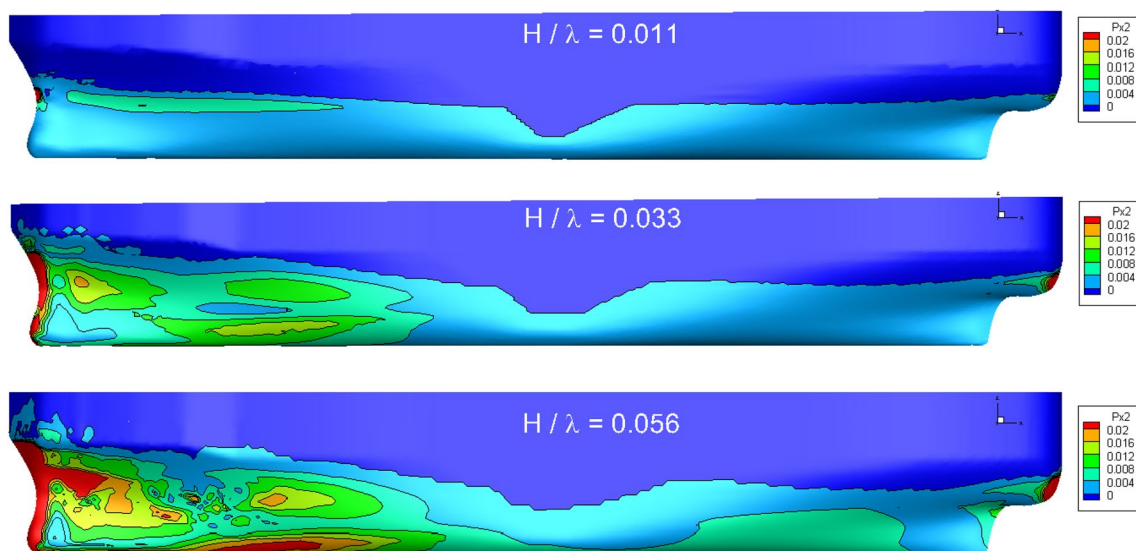


Fig. 19 Second harmonic amplitude of the x component of pressure for the case of $H/\lambda = 0.011, 0.033, 0.056$

second harmonic amplitudes of the x component of pressure for the case of $H/\lambda = 0.011, 0.033, 0.056$. With the increase of wave steepness, both first and second harmonic amplitudes increase, especially near the bow.

6 Conclusions

Ship motions and added resistance of the S175 containership under different wave steepness at a fixed wavelength are calculated by a RANS solver based on a finite-volume method in an unstructured grid. A level set function is employed to capture the free surface and ship motions are considered with the application of dynamic grids. The grid-dependence tests are performed to investigate the influence of grid size on the quality of incident wave propagation.

The non-dimensional amplitudes of heave and pitch and added resistance coefficients under different wave steepness agree well with the experimental data. This indicates that the present numerical method can take into account the influence of wave steepness with good accuracy.

It is shown that the higher harmonic components of surge force increase dramatically as the wave steepness increases which indicates the limitation of the application of second-order potential flow theory in high waves. For heave and pitch motion, higher harmonics are quite small compared to the first harmonics.

Very complicated transient wave patterns and hull pressure distributions are observed. The nonlinearity of resistance is closely related to the amplitude and phase of incident waves and ship motions and the interactions between them. The zeroth, first, and second harmonic amplitudes of pressure are plotted on the hull and the major part of resistance increase in steeper waves is found to be induced at the bow.

Acknowledgements This study is supported by the China Ministry of Education Key Research Project “Knowledge-based Ship Design Hyper-Integrated Platform II” (GKZY010004) and Institute of Advanced Sciences in Yokohama National University. The calculation was conducted in the Ship Flow Simulation Laboratory of Yokohama National University during the Student Exchange Program between YNU and SJTU sponsored by Japan Student Services Organization and the author(SC) thanks to the members of the laboratory.

References

- MEPC 62/24/Add.1 (2011) Amendments to the annex of the Protocol of 1997 to amend the International Convention for the Prevention of Pollution from Ships, 1973, as modified by the Protocol of 1978 relating thereto. IMO, London
- MEPC 65/22 (2013) 2013 interim guidelines for determining minimum propulsion power to maintain the manoeuvrability of ships in adverse conditions. IMO, London
- Nakamura S, Naito S (1977) Propulsive performance of a container ship in waves. *J Soc Nav Archit Jpn* 15:24–48
- Maruo H (1963) Resistance in waves. In: *Researches on seakeeping qualities of ships in Japan*. The Society of Naval Architects of Japan, Tokyo, pp 67–102
- Gerritsma J, Beukelman W (1972) Analysis of the resistance increase in waves of a fast cargo ship. *Int Shipbuild Prog* 19(217):285–293
- Salvesen N (1978) Added resistance of ships in waves. *J Hydronaut* 12(1):24–34
- Fang MC, Chen GR (2006) On the nonlinear hydrodynamic forces for a ship advancing in waves. *Ocean Eng* 33(16):2119–2134
- Liu S, Papanikolaou A, Zaraphonitis G (2011) Prediction of added resistance of ships in waves. *Ocean Eng* 38(4):641–650
- Faltinsen OM, Minsaas KJ, Liapis N, Skjoldal SO (1980) Prediction of resistance and propulsion of a ship in a seaway. In: *Proceedings of 13th Symposium on Naval Hydrodynamics*, Tokyo, Japan, pp 505–529
- Kim KH, Kim Y (2011) Numerical study on added resistance of ships by using a time-domain Rankine panel method. *Ocean Eng* 38(13):1357–1367
- Chen XB (2007) Middle-field formulation for the computation of wave-drift loads. *J Eng Math* 59(1):61–82
- Pan Z, Vada T, Han K (2016) Computation of wave added resistance by control surface integration. In: *Proceedings of the ASME 2016 35th International Conference on Ocean, Offshore and Arctic Engineering*, Busan, South Korea, Paper # OMAE2016-54353
- Chen S, Ma N, Gu X (2017) Numerical calculation of added resistance of ships in waves based on weakly nonlinear assumption. *J Shanghai Jiaotong Univ* 51(3):277–283
- Orihara H, Miyata H (2003) Evaluation of added resistance in regular incident waves by computational fluid dynamics motion simulation using an overlapping grid system. *J Mar Sci Technol* 8(2):47–60
- Ley J, Sigmund S, El Moctar O (2014) Numerical prediction of the added resistance of ships in waves. In: *Proceedings of the ASME 2014 33rd International Conference on Ocean, Offshore and Arctic Engineering*, San Francisco, USA, Paper # OMAE2014-24216
- Simonsen CD, Otzen JF, Joncquez S, Stern F (2013) EFD and CFD for KCS heaving and pitching in regular head waves. *J Mar Sci Technol* 18(4):435–459
- Sadat-Hosseini H, Wu PC, Carrica PM, Kim H, Toda Y, Stern F (2013) CFD verification and validation of added resistance and motions of KVLCC2 with fixed and free surge in short and long head waves. *Ocean Eng* 59:240–273
- Larsson L, Stern F, Visonneau M (2013) CFD in ship hydrodynamics—results of the Gothenburg 2010 workshop. In: *MARINE 2011, IV International Conference on Computational Methods in Marine Engineering: Selected Papers*, Springer Science & Business Media, pp 237–259
- Shen Z, Wan D (2013) RANS computations of added resistance and motions of a ship in head waves. *Int J Offshore Polar Eng* 23(04):264–271
- Hino T (1997) A 3D unstructured grid method for incompressible viscous flows. *J Soc Nav Archit Jpn* 1997(182):9–15
- Hino T (1999) An interface capturing method for free surface flow computations on unstructured grids. *J Soc Nav Archit Jpn* 1999(186):177–183
- Menter FR (1994) Two-equation eddy-viscosity turbulence models for engineering applications. *AIAA J* 32(8):1598–1605
- Spalart P, Allmaras S (1994) A one-equation turbulence model for aerodynamic flows. *Rech Aerosp* 1:5–21
- Hinatsu M, Hino T (2002) Numerical investigation of influence of surging motion on viscous flows around a Wigley hull running in incident waves. *ASME 2002 Joint US-European Fluids Engineering Division Conference*. American Society of Mechanical Engineers, New York, pp 923–929

25. Ohashi K, Sakamoto N, Hino T (2013) Numerical simulation of flows around kvlcc2 hull form with ship motions in regular waves. In: 5th International Conference on Computational Methods in Marine Engineering, Hamburg, Germany <https://www.researchgate.net/publication/265694583>
26. Sakamoto N, Ohashi K (2012) Unsteady wake analysis for Series60 ($C_B = 0.6$) pitching and heaving in regular head seas by URANS. Symposium papers of the 26th computational fluid dynamics. The Japan Society of Fluid Mechanics, Tokyo, pp D09–2
27. Joncquez S, Bingham H, Andersen P (2008) Validation of added resistance computations by a potential-flow boundary-element method. In: 27th Symposium on Naval Hydrodynamics, Seoul, Korea, pp 1400–1410
28. Larsson L, Stern F, Visonneau M (2013) Numerical ship hydrodynamics: an assessment of the Gothenburg 2010 workshop. Springer Science & Business Media, New York